Magnetometamaterials: Metamaterials with Tunable Magnetic Matter Conductivity

Roozbeh Abedini-Nassab*

Faculty of Mechanical Engineering, Tarbiat Modares University, P.O. Box 14115-111, Tehran, Iran

(Received 30 September 2021; revised 28 November 2021; accepted 6 December 2021; published 18 January 2022)

The transport of tiny particles is of great interest in the field of lab-on-a-chip. Here, by drawing inspiration from electric materials, we introduce magnetometamaterials, which, as opposed to electrons, transport magnetic particles (i.e., matter). The proposed metamaterial is composed of lithographically patterned disk-shaped micromagnets arranged in rows forming linear magnetic tracks on a silicon substrate. It is shown that by applying an external rotating magnetic field with the right frequency, the particles move along the magnetic tracks. The magnetic matter transport rate (i.e., magnetic matter conductivity) is tuned by adjusting the external magnetic field. We show that the particle transport is similar to the classical electron transport through a periodic lattice. At low frequencies, similar to the electrons at low temperatures, the particles move in closed loops around single magnets, resulting in an insulating regime. At higher frequencies, similar to the electrons at higher temperatures, some particles show the same behavior (i.e., move in closed loops); however, some others move along the magnetic tracks (i.e., demonstrate open trajectories). This behavior resembles a magnetic matter semiconductor. At even higher frequencies, all the particles show open trajectories along the magnetic tracks, and the device resembles a magnetic matter conductor. We define the operational ranges, both theoretically and experimentally, for both one- and two-dimensional magnetometamaterials. We show that, in an appropriate vertical bias field, the two-dimensional magnetometamaterials can transport the particles in arbitrary paths. The proposed metamaterial in this work can be used in designing circuits for transporting particles with crucial applications in biomedical engineering.

DOI: 10.1103/PhysRevApplied.17.014020

I. INTRODUCTION

The precise manipulation and transport of microparticles has created a great deal of interest in the field of lab-on-a-chip [1–6]. For example, biologists are now interested in single-cell analysis (SCA) of the highly heterogeneous cell populations in tissues to understand the single-cell-level phenomena, playing significant roles in diseases that cannot be addressed by the average-based bulk-level analysis methods [7]. By employing SCA tools, the cell heterogeneity, the rare cells, and the infrequent biological processes that usually define the patient destiny in diseases such as cancer or HIV can be studied. Multiple SCA tools and particle manipulation techniques are already developed and have resulted in fundamental achievements in understanding cellular behavior [7,8], cancer biology [9–11], infectious diseases [12–15], and transplantation [16,17].

Flow cytometry and droplet-based microfluidic are two well-known flow-based single-cell analysis tools [18–20]. However, in these methods, the particles of interest typically move at high speeds in front of a detector, and thus studying their dynamic behavior is limited. Towards this goal, cells are usually assembled in arrays of microchambers. These techniques are categorized as groups of (i) microengraving tools [21], (ii) hydrodynamic sorters [22,23], (iii) acoustic sorters [24,25], and electromagnetic sorters [26–28]. But these techniques usually suffer from one or more disadvantages of limited cell numbers, complicated systems, lack of biocompatibility, and so on.

The microengraving technique (i.e., a chip composed of numerous microwells) is one of the simplest methods for assembling cells in arrays of microwells. After dispersing the cells in the microwells, various dynamic analyses, including drug screening, can be performed. However, the movement of the particles after dispersion is not possible. Also, extraction of the cells from their microwells requires manual or robotic pipetting, which may be time consuming. In hydrodynamic sorters, microchannel geometries in the microfluidic chips are designed to capture single particles in the trap sites. The number of cells in the commercialized tools based on this technique is usually limited. Also, applied shear stress to the trapped cells may affect the cell behavior and viability. Additionally,

*abedini@modares.ac.ir

extraction of the cells from the chip after analysis is challenging. The acoustic sorters are considered as promising particle transport tools; however, manipulating a subset of particles among the others is usually challenging. Also, in order to transfer the waves, the microfluidic chip usually needs to be of hard material such as glass or similar, limiting the options. The electromagnetic sorters use electric, magnetic, or optical forces to move the particles. In electrical methods (electrophoresis or electrowetting), the wiring system is normally complicated. In the methods based on magnetic forces, external magnets or coils [29] and embedded microcoils [30] provide the driving force for the particles. The unwanted heat generated by the current-carrying coils and the complicated wiring systems are considered drawbacks of these tools. The optical tweezers accurately manipulate particles; however, the high-frequency electromagnetic field applied to the bioparticles may be problematic. Also, in opaque media, optical particle transport is challenging. Thus, innovating tools capable of precisely manipulating a sufficient number of particles in an automated manner that overcomes the mentioned limitations are needed.

Engineering metamaterials with desirable properties that usually go beyond those of the ingredients is considered one of the interesting fields in recent years. Although this discipline emerged from electromagnetism, it now addresses so many aspects in the fields of electromagnetics, optics, acoustics, etc. [31–35]. Lab-on-a-chip is one of the fields in which metamaterials have found potential applications [36–38]. In most of these works, a metamaterial is embedded into a microfluidic chip to achieve desired outcomes. We believe on-chip particle manipulation can be fundamentally enhanced by engineering and employing specific metamaterials to answer the need mentioned above.

Researchers have always shown interest in magnetophoretic particle manipulation techniques [39,40]. This phenomena is used in manipulating magnetic nanoparticles [41,42], microparticles [43,44], and cells [45,46], as well as in magnetic based microfluidic devices [47,48]. Previously, the dynamic trajectory of particles around single magnetic disks in an in-plane magnetic field is studied [49,50]. In other works, particle transport through a periodic magnetic array has been studied. In some studies, a two-dimensional (2D) rotating field perpendicular to the substrate is used to manipulate the particles [51,52]. In this method, one-dimensional (1D) particle transport is achieved. The particle transport in disordered landscapes results in 2D particle transport, but with no precise control on the particle trajectories [53]. The version derived with a three-dimensional (3D) magnetic field, where particle transport in a plane is carried out, has also been proposed [54]. But, the particle trajectory in this method is not smooth and precise control over the particle position is not possible.

Here, we propose a metamaterial, which operates fundamentally differently compared to the available methods and smoothly transports a large number of particles (i.e., matter) in parallel in both 1D and 2D paths. Drawing inspiration from electric materials, we design a material with tunable magnetic matter conductivity, where, as opposed to electrons, magnetic matters such as magnetic beads and magnetized cells are transported. This metamaterial, called magnetometamaterial, is composed of micromagnets fabricated on a silicon chip spaced with a gap of a specific size. The schematic of the proposed material with a microparticle on it as well as the experimental setup are illustrated in Fig. 1.

A rotating in-plane magnetic field produced with the four coils shown in Figs. 1(b) and 1(c) is applied to the metamaterial, providing the driving force for the movement of the particles. The rotating field is produced by applying two sine waves with 90° phase difference, as illustrated in Fig. 1(d), to coil pairs *A* and *C*, and *B* and *D*, respectively. The resulting magnetic field directions at various time points are illustrated in Fig. 1(d) with black arrows. With the invention of the 3D-printed coils [55], it is also possible to replace the coils with tiny ones. The conductivity of this material is tunable by adjusting the frequency of the applied external magnetic field.

We show that this metamaterial can be biased to operate as an insulator, in which no magnetic particle moves, a semiconductor, in which some magnetic particles are transported, or a conductor, in which all particles are carried. In fact, we demonstrate that the operation of the introduced metamaterial interestingly mimics the classical electron transport in a lattice. We show that applied frequency plays the role of the temperature in electric lattices. At low frequencies, the magnetic particles are at "equilibrium" with the energy well produced by the magnetic disks. Thus, similar to the electrons in an insulator, the particles remain around their initial disk. But, at high frequencies, the particles are not at "equilibrium" with the energy wells. In analogy to electrons that are not at thermal equilibrium and move to the other atoms, the particles move to the neighboring magnetic microdisks. This behavior is the reverse of the action seen in previous works, where high frequency results in overdamping and insulation [50,56], and it is being described here.

We present the operation of both 1D and 2D magnetomaterials. The magnetic field introduced to the 2D version of the metamaterial is different from the one in the other works, being composed of a rotating in-plane field and a tuned pulse waveform vertical field. This magnetic field results in an energy distribution suitable for precise particle manipulation in a much controllable manner, compared to the previous works. We also demonstrate that the particle current in the proposed materials obeys a law similar to Ohm's law in electrical conductors.

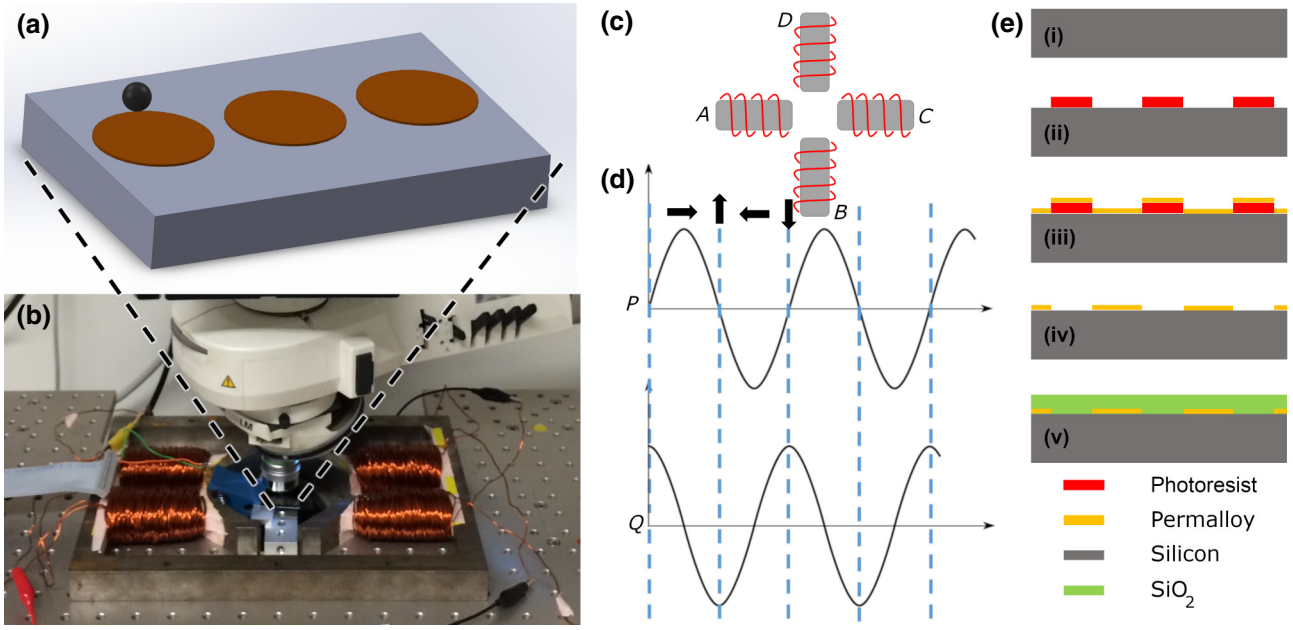

FIG. 1. Experimental setup, magnetic fields, and the fabrication steps are illustrated. (a) Schematic of the proposed magnetometamaterial, where a single magnetic particle (black sphere) is on the perimeter of a micromagnet (brown disks) on a chip, is shown. (b) The experimental setup is illustrated, where the magnetometamaterial is mounted in between four coils under a microscope. An extra vertical coil is added underneath the stage for providing the vertical bias field when needed. (c) A schematic of the top view of the coils is shown. (d) Waveforms of the applied currents are shown. Waveform P is applied to the coils A and C, which are electrically connected in series. Waveform Q is applied to the coils B and D, which are electrically connected in series. Black arrows at each timepoint depict the direction of the produced magnetic field in between the coils in (c). (e) A schematic of the fabrication process is shown. (i) A silicon wafer is used as the substrate. (ii) Photoresist is patterned. (iii) Permalloy is deposited on the chip. (iv) After liftoff the disks are formed on the chip. (v) The whole chip is covered with silicon dioxide.

II. MATERIALS AND METHODS

To fabricate the proposed material, starting with a silicon substrate, a double layer of P-20 (Shin-Etsu MicroSi, Pheonix, AZ) adhesion promoter and NFR16-D2 (JSR Micro Inc., Sunnyvale, CA) is spin coated. After a prebake step at 115 °C for 60 s the chips are ultraviolet exposed for 12 s at an illumination power of 13.5 mW at a wavelength of 365 nm (Karl Suss MA6/BA6), and then are developed with Microposit MF-319 developer (Shipley, Marlborough, MA). After rinsing, using an electron-beam metal evaporator (Kurt Lesker PVD 75) a 5-nm/150-nm thin-film stack of Ti/permalloy ($Ni_{80}Fe_{20}$) is deposited on the chips. Then, the chips are coated with a 200-nm thin film of SiO_2 using a plasma-enhanced chemical vapor deposition (PECVD) (Advanced Vacuum Vision 310) machine. These steps are depicted in the schematic in Fig. 1(e).

The experiments are performed using magnetic beads with mean diameters of 2.8 μm (Dynabeads M-280) and 5.7 μm (Spherotech CM-50-10). The coils shown in the experimental setup in Fig. 1 are powered by programmable power supplies (Kepco BOP 20-5 M), and controlled by a customized LabVIEW program (National Instrument).

We simulate the particle trajectory and the energy landscape, as explained in detail elsewhere [56,57], using semianalytical approximations. We model the thin disks exposed to an external uniform magnetic field with uniformly magnetized ellipsoids or oblate spheroids with semiprincipal axes of length a, b, and c along the x, y, and z directions, respectively. The analytical expression for the magnetic potential inside and outside them, when the applied external magnetic field is along the x direction, is given by [58]

$$\varphi_{\text{out}} = F_1(\xi)F_2(\varsigma)F_3(\zeta) \times \left[C_1 + C_2 \int_{\xi}^{\infty} \frac{ds}{\sqrt{(s+a^2)(s+b^2)(s+c^2)}(s+a^2)}\right], \tag{1}$$

$$\varphi_{\text{in}} = C_3 F_1(\xi)F_2(\varsigma)F_3(\zeta), \tag{2}$$

where $F_1 = \sqrt{\xi + a^2}$, $F_2 = \sqrt{\varsigma + b^2}$, and $F_3 = \sqrt{\zeta + c^2}$. Using boundary conditions at the surface of the ellipsoid $\{\varphi_{\text{out}} = \varphi_{\text{in}}$ and $\mu_0[(\partial\varphi_{\text{out}}/h_\xi \partial\xi)] = \mu_i[(\partial\varphi_{\text{in}}/h_\xi \partial\xi)]\}$ we determine coefficients, C_1, C_2, and C_3. Here μ_0 and μ_i are magnetic permeability of the surrounding medium (assuming to be vacuum and $\mu_0 \ll \mu_i$) and the magnetic ellipsoids, respectively. The fields outside and inside the ellipsoids and the magnetic dipole density on the surface of the

ellipsoids can be derived by

$$\vec{H}_{\text{out}} = -\nabla\varphi_{\text{out}}, \quad \vec{H}_{\text{in}} = -\nabla\varphi_{\text{in}}, \tag{3}$$

$$\sigma_M = (\vec{H}_{\text{out}} - \vec{H}_{\text{in}}).\hat{n}, \tag{4}$$

with n standing for the local outward normal of the ellipsoid curvature. Then we find the resulting magnetic potential:

$$\varphi_{\text{out}} = \frac{\mu_0}{4\pi}\int \frac{\sigma_M}{|r - r_s|}ds, \tag{5}$$

where r and r_s are the observation and source position vectors, respectively. The magnetic force acting on magnetic particles can be derived using $\vec{F}_{\text{mag}} = \mu_0(\vec{m}\cdot\nabla)\vec{H}$, where H is the magnetic field applied to them. We treat each magnetic particle as a point dipole with the dipole moment of $\vec{m} = \chi V\vec{H}$, where V and χ are the volume and magnetic susceptibility of the particles.

Overdamped first-order equations of motion can model the motion of the small particles in aqueous fluids. The velocity of the particle is assumed to be

$$\vec{V} = \frac{\vec{F}_{\text{mag}}}{6\pi\eta a}, \tag{6}$$

where the denominator is Stoke's friction coefficient for a sphere in a quiescent fluid and η is the surrounding medium viscosity. Finally, the particle trajectory is predicted by integrating the velocity in a forward difference scheme, $r_i = r_{i-1} + v_{i-1}\,\Delta t$, in which r_{i-1}, r_i, and v_{i-1} are the particle position vectors at the $i-1$th timestep, ith timestep, and the velocity at the $i-1$th timestep, respectively. Δt is the timestep to be chosen to achieve numerical convergence.

III. RESULTS

Micromagnets exposed to an external in-plane magnetic field (H_{ext}), produce magnetophoretic energy wells on both sides of their periphery, at which magnetic particles are. This phenomenon is shown in the energy simulation results depicted in Fig. 2(a), in which the blue areas represent the energy wells. By rotating the external field, the energy wells rotate around the magnets. At low frequencies, below a critical frequency f_{cs1}, (i.e., phase-locked regime) the balance between the magnetic and drag force lets the particle follow the rotating energy wells and move synchronously around the micromagnet, with a fixed phase lag θ_{lag}, depicted in Fig. 2(a). The particle trajectory at this regime is shown in Fig. 2(e) (also see Movie S1 within the Supplemental Material [59]). Increasing the frequency

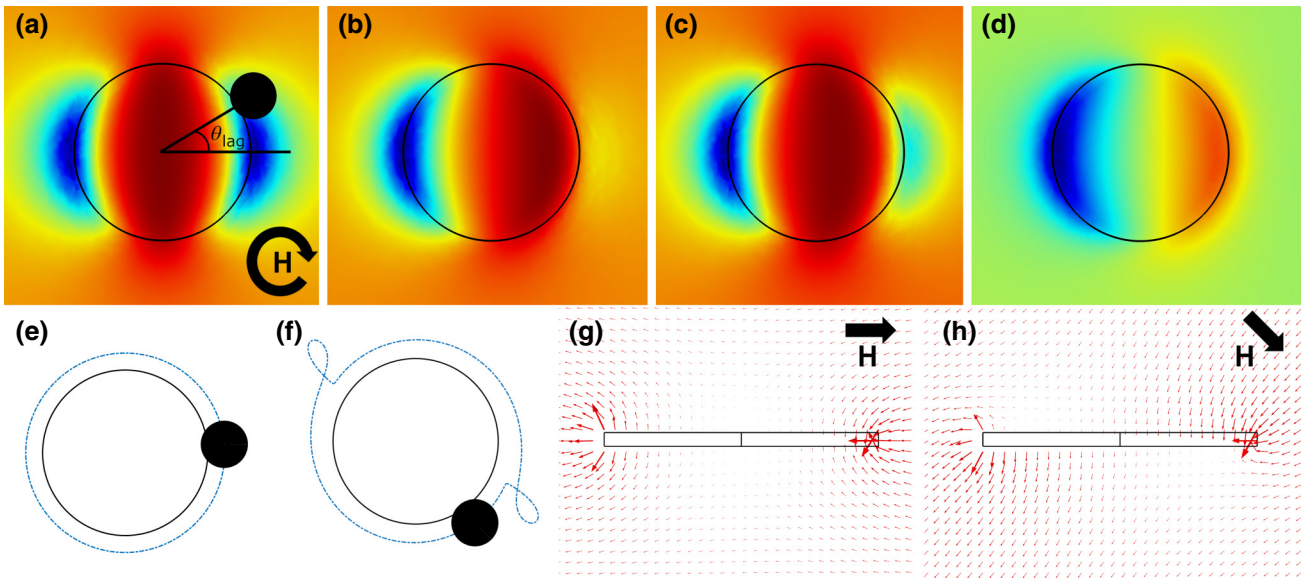

FIG. 2. Energy landscape and particle-trajectory simulation results for a single micromagnet are shown. (a) The energy landscape in an in-plane external magnetic field of 100 Oe, (b) in a 3D external magnetic field with both in-plane and vertical bias components of 100 Oe, (c) in a 3D external magnetic field with in-plane and vertical bias components of 150 and 50 Oe, respectively, (d) and in a 3D external magnetic field with in-plane and vertical bias components of 50 and 150 Oe, respectively, are illustrated. The circular arrow depicts the rotation of the external magnetic field. θ_{lag} is the phase lag between the external magnetic field and the particle position. The blue and red areas represent the regions with low and high energies, respectively. The large and small circles stand for the disk and the particle, respectively. (e) The particle trajectory at the phase-locked and (f) the phase-slipping regimes are illustrated. The blue lines in (e) and (f) represent the particle trajectories. The applied magnetic field frequencies in (e) and (f) are 0.1 and 1.2 Hz, respectively, with an intensity of 100 Oe. A side view of the magnetic field distribution corresponding to the energy distribution in (g),(a) and (g),(b) are shown. In (g) and (h) the black arrows depict the external magnetic field direction. The disk and particle diameters are 10 and 2.8 μm, respectively. Also, see Movies S1 and S2 within the Supplemental Material [59].

increases the phase lag; however, at frequencies higher than the critical frequency, the phase lag reaches 45°, and the magnetic particle can no longer follow the rotating energy well (i.e., the phase-slipping regime). At this regime, the particle slips out of the circular path around the magnet and follows the next approaching energy well [50] (see Fig. 2(f) and Movie S2 within the Supplemental Material [59] for the particle trajectory). The applied magnetic field frequencies in the examples in Figs. 2(e) and 2(f) are 0.1 and 1.2 Hz, respectively. The magnetic field intensity is 100 Oe. Based on our simulation results (not shown here), the stronger external magnetic field deepens the energy wells on disk poles but does not change the overall energy distribution.

Superimposing a vertical bias magnetic field turns one of the energy wells into an energy barrier [see Fig. 2(b)]. Since the magnetic energy is proportional to the magnetic field squared, a plot of the magnetic field helps to understand this phenomenon. Figures 2(g) and 2(h) illustrate a side view of the magnetic field around the disk, in an in-plane external magnetic field and a 3D magnetic field, respectively. The magnetic field around the poles in an in-plane field is symmetric [see Fig. 2(g)]; however, by applying a vertical bias field it becomes asymmetric [see Fig. 2(h)]. Both vertical and horizontal components of the magnetic field in Figs. 2(b) and 1(h) are 100 Oe. Applying a vertical field weaker than the horizontal field is not sufficient for removing the energy well [see Fig. 2(c) where the horizontal and vertical magnetic field components are 150 and 50 Oe, respectively]. Application of a vertical magnetic field component stronger than the horizontal magnetic field component narrows the energy barrier and shifts it more towards the disk edge [see Fig. 2(d) where the horizontal and vertical magnetic field components are 50 and 150 Oe, respectively] compared to the case shown in Fig. 2(b).

A. One-dimensional micromagnet array

When more than a single micromagnet are arranged in a row (see Fig. 3), the superposition of their forces (neglecting the effect of magnets on each other) can be taken into account. At frequencies lower than a critical frequency, f_{cm}, the particle follows the energy well and rotates around a single micromagnet [see Fig. 3(a) for the energy simulation results and Figs. 4(a) and 4(e) for the simulation and experimental trajectories, respectively]. We call this case the "insulating regime," in which the designed metamaterial does not transport particles (i.e., it behaves as an insulator). At frequencies higher than f_{cm}, because of the large phase lag, in between the two disks, the particle is far from its leading energy well [labeled 1 in Fig. 3(b)] with an energy barrier in between, compared to the energy well circulating the next magnet [labeled 2 in Fig. 3(b)]. Thus, the particle moves toward the energy well on the next magnet

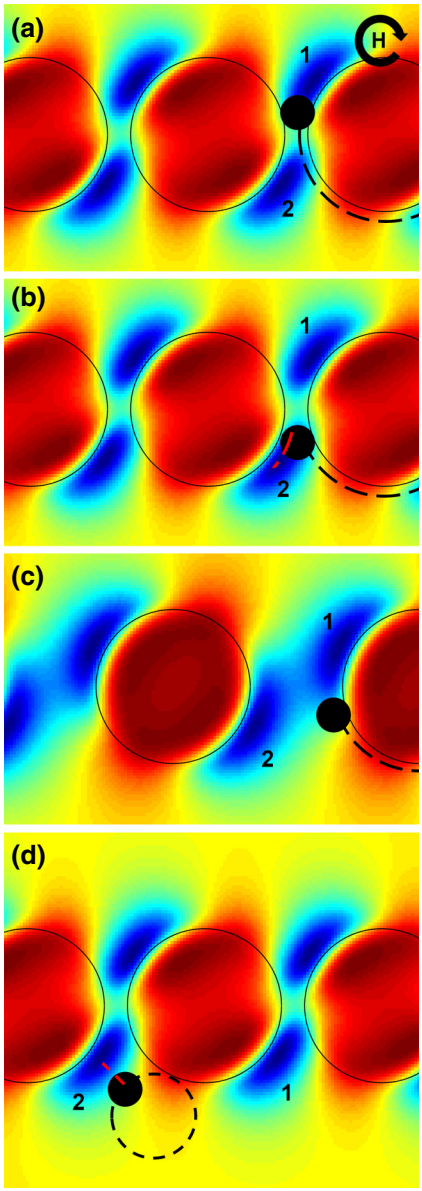

FIG. 3. Energy simulation results for the proposed metamaterial are shown. (a) At frequencies lower than f_{cm}, where the phase lag is small, the particle rotates around a single micromagnet. The dashed black line depicts the particle trajectory. (b) At frequencies higher than f_{cm}, where the phase lag is large, the particle moves to the next magnet. The dashed black line shows the particle trajectory around the first magnet, while the dashed red line depicts the trajectory around the second magnet. (c) When the gap size between the magnets is large, the particle circulates a single magnet. The dashed black line shows the particle trajectory. (d) At frequencies higher than f_{cs}, the particle moves from one magnet to the next one. Here, as opposed to a circular slipping out path (dashed black line), the particle moves along the dashed red line. Numbers 1 and 2 stand for the leading energy well in the first micromagnet and the energy well on the next micromagnet, respectively. The circular arrow depicts the direction of the external magnetic field rotation. The field intensity is 100 Oe. The disk and particle diameters are 10 and 2.8 μm, respectively.

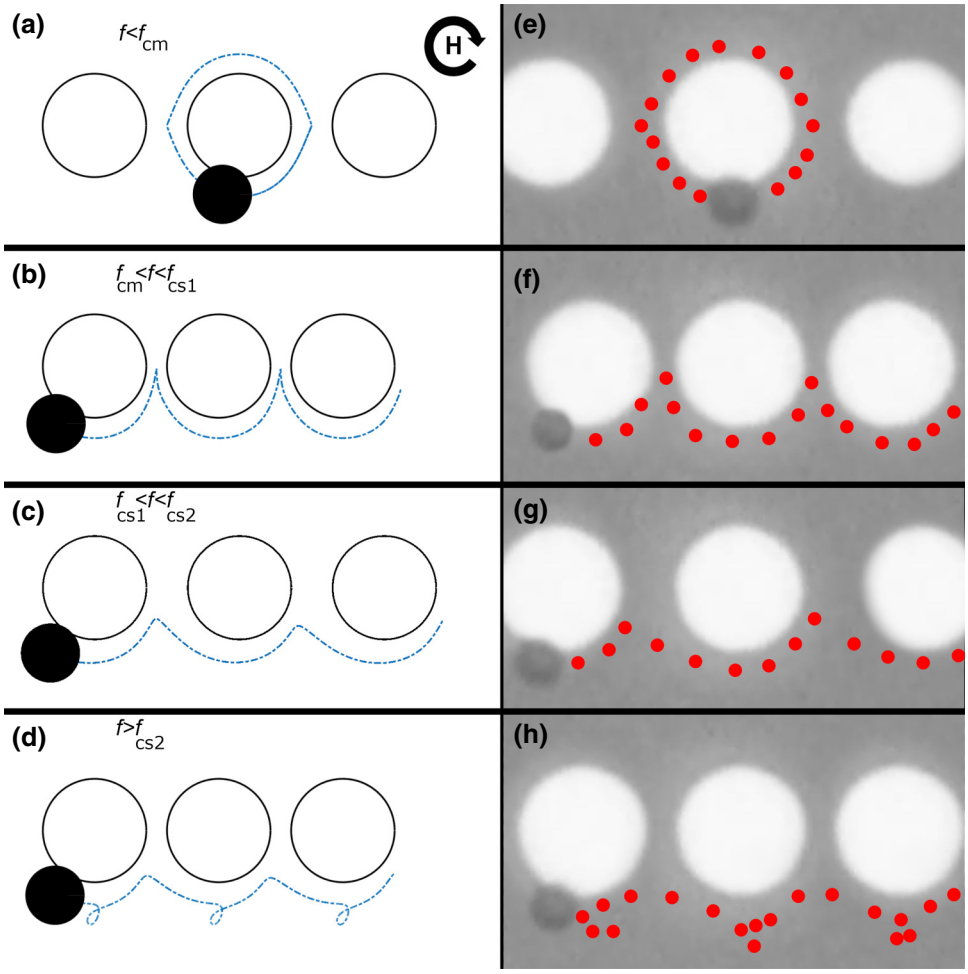

FIG. 4. Particle trajectories in the proposed metamaterial are illustrated. (a)–(d) Simulation results for the particle trajectories are shown with the dashed blue lines. (e)–(h) Experimental results are illustrated with the dotted red lines. The circular arrow depicts the direction of the external magnetic field rotation. The disk and particle mean diameters are 6 and 2.8 μm, respectively. The applied magnetic field frequencies in *a*, *b*, *c*, and *d* are 0.1, 0.3, 0.9, and 1.2 Hz, respectively, with the intensity of 100 Oe. The frequencies in the experiments are the same as the ones used in the simulations.

[labeled 2 in Fig. 3(b)]. The simulation and experimental results for this case are shown in Figs. 4(b) and 4(f), respectively. f_{cm} depends on factors including particle size, particle magnetization, gap size, etc. For example, the energy simulation result in Fig. 3(c) shows that a large gap size in between the magnets results in an energy barrier between the particle and the next magnet, preventing the particle from moving to that magnet. Thus, since in reality, these parameters are different among various particles and magnets on the chip (i.e., they are slightly different in size and magnetization), some particles are transported along the magnetic tracks while others are not. We call this regime the "semiconducting regime." We can tune the conductivity of the proposed material at this regime by adjusting the applied frequency: the higher the frequency, the higher the conductivity.

Two different conducting regimes are observed at higher frequencies. At frequencies higher than the ones of the semiconductor regime, all the particles move to the next magnets, representing the conducting regime, called the "nonslipping conducting regime." At even higher frequencies (i.e., $f > f_{cs1}$), the particle of interest slips out of the given energy well. When only a single magnet exists [see Fig. 2(c)], the particle moves to the next coming energy well circulating that magnet. However, in the case of the proposed metamaterial in this work, the energy well circulating the next magnet is closer to the slipping particle, and thus the particle moves toward the next magnet [see Fig. 3(d) for the energy simulation results and Figs. 4(c) and 4(g) for the simulation and experimental trajectory results, respectively]. This case represents the "slipping conducting regime". In both defined conducting regimes, the proposed metamaterial transports particles along the magnetic tracks. At even higher frequencies (i.e., $f > f_{cs2}$), the number of slipping outs increases, and something similar to what is shown in Fig. 2(c) is observed, before the particle moves to the next magnet [see Figs. 4(d) and 4(h) for the simulation and experimental trajectories, respectively]. The applied magnetic field frequencies in Figs. 4(a)–(d) are 0.1, 0.3, 0.9, and 1.2 Hz, respectively. The frequencies in the experiments are the same as the ones used in the simulations.

By further increasing the applied frequency ($f > f_{cs3}$) (e.g., 20 Hz, in the case of our experiments with the magnetic disk and bead diameters of 10 and 2.8 μm, respectively), the particle oscillates around a fixed point

on the perimeter of the micromagnet. The origin of this phenomenon can be caused by defects in the micromagnets (e.g., magnetization defects or imperfect geometries). We call this regime, in which the particle is trapped on a pinning site, the "deep insulating regime." At this regime, the metamaterial again behaves similar to an insulator material.

The phase diagrams in Fig. 5 illustrate the percentage of magnetic particles moving along the magnetic tracks on the proposed magnetometamaterial (i.e., conductivity), as a function of the gap size between the disks and the applied external field frequency. The hand-drawn lines in this figure are used as guides to the eyes, which define the boundaries of their respective transport regimes. The solid line stands for the boundary for the conducting regime, while the dotted line depicts the boundary for the insulating regime. The area in between the two lines represents the semiconducting regime. The other insulating regime at high frequencies (i.e., $f > 15$ Hz) is not shown in this figure. We repeat this experiment for particles with mean sizes of 2.8 and 5.7 μm, the results of which are illustrated in Figs. 5(a) and 5(b), respectively. In each case, the trajectories of at least 20 beads are recorded.

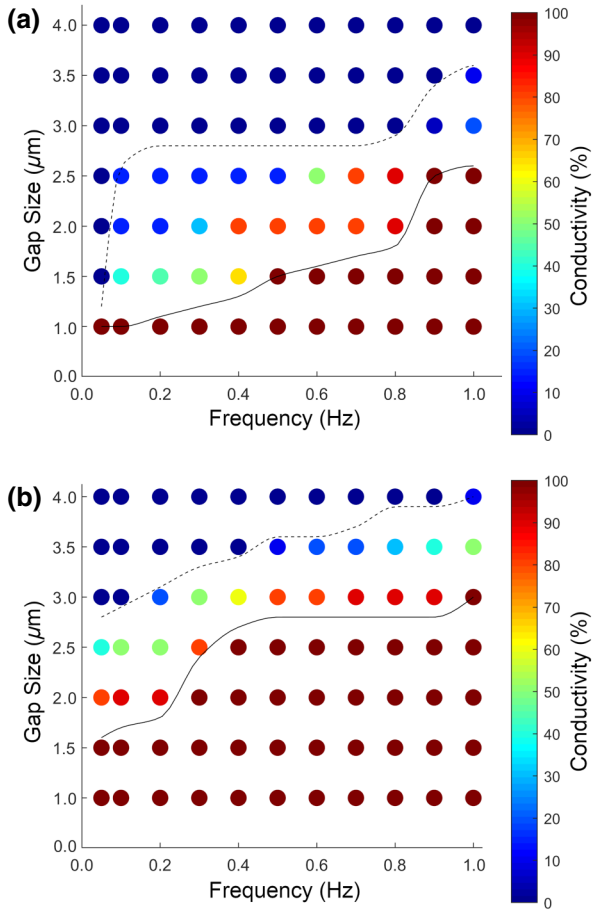

FIG. 5. The gap size versus frequency phase diagram for the magnetometamaterial is shown. The boundaries of the conducting and insulating regimes for particles are represented with solid and dashed lines, respectively. The area between the two lines stands for the semiconducting regime. The disk diameter is 6 μm, and the particle mean diameters are (a) 2.8 μm and (b) 5.7 μm. The magnetic field intensity is 100 Oe.

The particle trajectory and the conductivity of the magnetometamaterial depend on various parameters, including the particle diameter, the magnetic susceptibility of the particle, the viscosity of the surrounding fluid, and the magnetic disk diameter. The effect of the first three parameters can be seen in Eq. (6). The particle diameter and the viscosity of the surrounding fluid have a direct effect on the drag force and thus lower the critical frequencies, increasing the magnetometamaterial conductivity at low frequencies. The experimental results in the phase diagrams illustrated in Fig. 5 confirm this discussion about the effect of the particle diameter. The magnetic susceptibility of the particle increases the magnetic force, and thus increases the critical frequencies. Hence, the conductivity of the magnetometamaterial is inversely proportional to the magnetic susceptibility of the particles. But the effect of the disk diameter may not be obvious in Eq. (6). Since the position of a particle circulating a magnetic disk is synced with the external magnetic field, in a given time, the

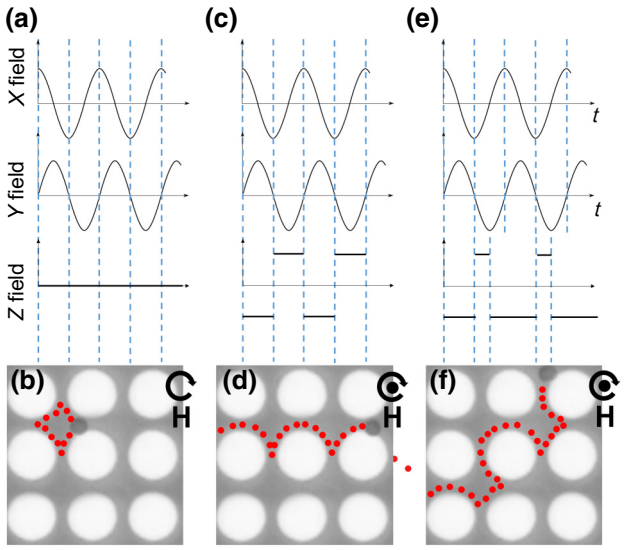

FIG. 6. Two-dimensional magnetometamaterials. (a) The magnetic field components and (b) the experimental particle trajectory when the z component is zero is presented. (c) The magnetic field components for an (d) open-loop particle trajectory are shown. (e) The magnetic field components for a (f) diagonal particle trajectory are depicted. The red dotted lines stand for the experimental particle trajectories. The circular arrow and the black circle stand for the external field rotation and the vertical bias, respectively. The operating frequency in these examples is 0.3 Hz. Both the horizontal and vertical components of the applied magnetic fields are 70 Oe.

particle needs to travel a larger perimeter around a larger magnetic disk compared with that circulating a smaller magnetic disk. That means in a given frequency, the particle travels a greater distance (i.e., moves at higher speed) around a larger disk, which results in a stronger drag force, compared with the one circulating a smaller disk. Thus, the conductivity of the magnetometamaterial is directly proportional to the disk size. This finding is supported by our simulation results (not shown here).

B. Two-dimensional micromagnet array

In addition to the 1D material introduced in the previous section, we also study the particle transports on 2D materials. When an in-plane rotating field, similar to the one used in the one-dimensional array design, is applied to a 2D micromagnet array, closed-loop particle trajectories show up. Our simulation and experimental results show that at low frequencies, particles circulate a single disk (not shown). This behavior is similar to the case of $f < f_{cm}$, explained above [see the red dotted line in Fig. 4(a)]. However, by increasing the external magnetic field frequency (e.g., 0.3 Hz in the example shown in Fig. 6), the particle moves from the first magnet to the next one in both x and y directions, every quarter of the time period. The waveform and the resulting closed-loop particle trajectory of this case are shown in Figs. 6(a) and 6(b), respectively. The red dots in Fig. 6(b) depict the particle trajectory extracted from our experiments.

The problem of forming a closed-loop particle trajectory, even after increasing the frequency in 2D design, arises from the fact that magnetized particles periodically switch between the north and south poles without penalty. This behavior is shown in Figs. 7(a)–7(d), where simulation results for four sequential time points, when the external field rotates clockwise, are illustrated. In this figure, the particle experimental trajectory is overlaid on the energy distributions by the red dots.

Superimposing a vertical field bias turns one of the energy wells into an energy peak. As shown in Figs. 7(e)–7(h), corresponding to four sequential time points in half a period, in an always-on vertical bias superimposed to a rotating in-plane field, single energy wells circulate single disks. But open trajectories can be achieved by applying a tuned rectangular waveform as the bias vertical magnetic field. As demonstrated in Fig. 6(d), particles move in the positive x direction when a clockwise in-plane rotating field is superimposed with a square wave,

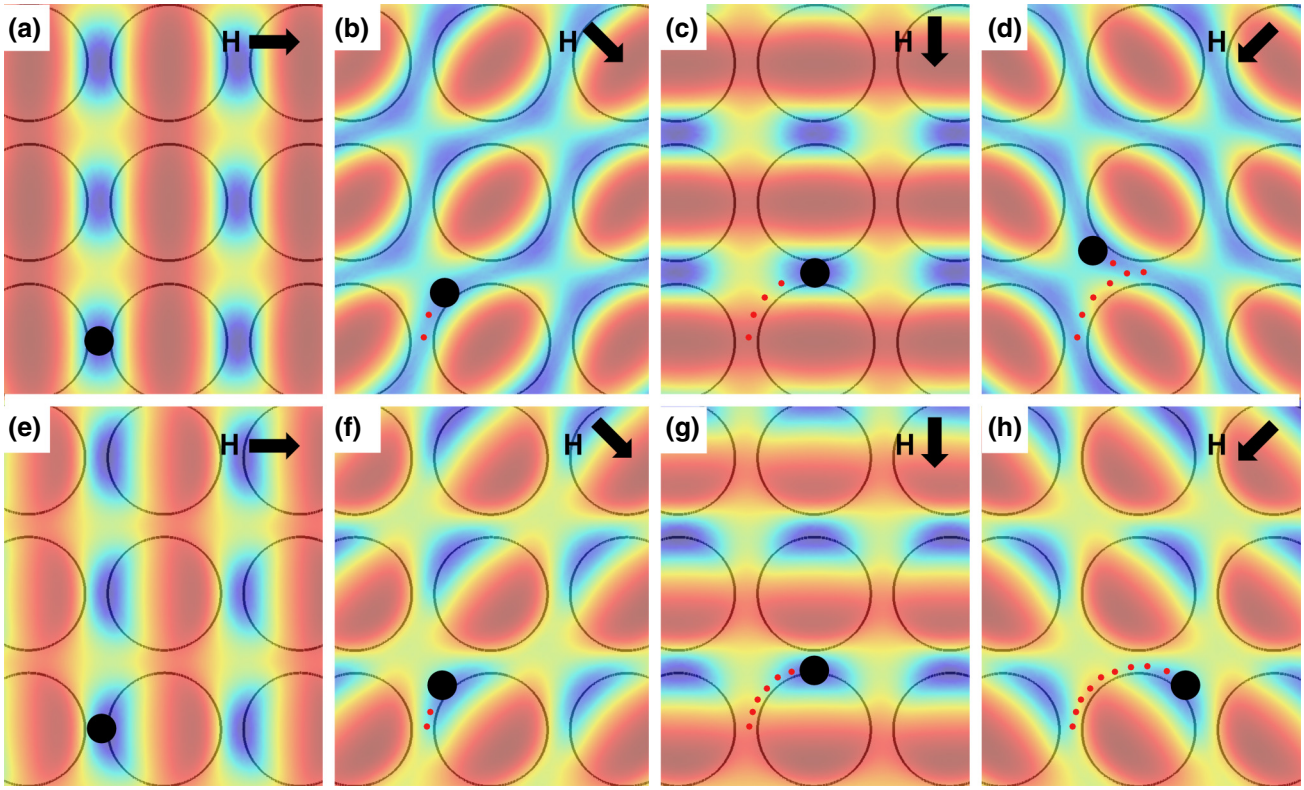

FIG. 7. Simulation results for a two-dimensional magnetometamaterial are illustrated. (a)–(d) An in-plane external magnetic field is applied. (e)–(h) An in-plane external magnetic field superimposed with a vertical field bias is applied. Blue and red areas stand for the low-energy and high-energy regions. Black arrows depict the field direction in each panel. The black circle stands for a particle position, and the red dotted lines are overlaid experimental trajectories, at the operating frequencies of 0.3 Hz. Both the horizontal and vertical components of the applied magnetic fields are 70 Oe.

the timing of which is shown in Fig. 6(c). The experimental results shown in this figure confirm our simulation predictions.

Other particle trajectories can be obtained by tuning the magnetic field components too. For example, by applying an asymmetric rectangular waveform as the vertical bias field, it is possible to achieve diagonal trajectories. Towards this goal, we apply the waveforms shown in Fig. 6(e), which resulted in the experimental trajectories shown in Fig. 6(f). Thus, the proposed 2D micromagnet array allows us to transport particles in various directions in a controlled manner. In Movie S3 within the Supplemental Material [59] a sample particle trajectory is shown.

Although superimposing an appropriately tuned bias vertical field adds a little bit to the power supply complexity, it can result in a more reliable particle transport. This achievement is due to the elimination of one of the magnetic disk poles, leaving only one pole near the particle to follow. Thus, the particle may not switch back to the wrong energy well. To systematically study the particle transport properties, we define $\beta = r_p/G$, as a dimensionless parameter, where r_p and G stand for the particle radius and the size of the gap between the disks, respectively. At frequencies in the range of $f_{cm} < f < f_{cs3}$, we observed open trajectories (i.e., conducting regime) for $\beta \geq 0.35$. At too low frequencies (i.e., $f < f_{cm}$) the particle circulates the perimeter of a single disk, and at too high frequencies (i.e., $f > f_{cs3}$) the particle does not move. For $\beta < 0.35$, the gap is too large for the particle to move from one magnet to the next one, and as a result, close trajectories are observed. Thus, for a magnetometamaterial to operate well, one needs to choose an appropriate β.

Analyzing the velocity of the particles as a function of the applied magnetic field frequency represents the similarity between the current of magnetic particles and Ohm's law in electrical circuits. As illustrated in Fig. 8, in appropriate driving frequencies, the particles move exactly two array periods in each magnetic field rotation cycle, demonstrating the linear relationship between the frequency and the magnetic particle current. The experimental data in this range overlap the black line in Fig. 8, which is used as a guide to the eye. At higher frequencies though, the particles enter the phase-slipping regime, the experimental data do not match with the black line and the analogies with Ohm's law breaks down. The experiments are repeated for particles with mean diameters of 2.8 and 5.7 μm. At least 20 trajectories in each experiment are recorded.

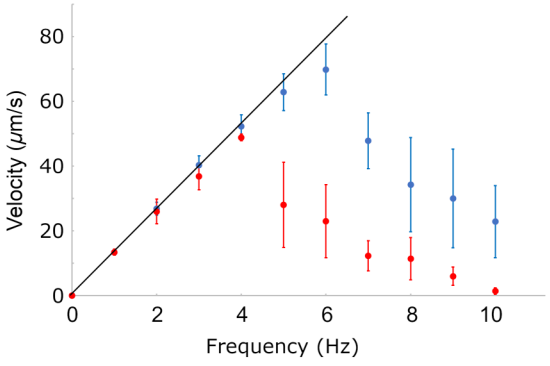

FIG. 8. Particle conduction. The velocity versus frequency relationship for the particle motion are illustrated. The blue and red dots stand for the particles with mean diameters of 2.8 and 5.7 μm, respectively, with the trajectory shown in Fig. 6(d).

IV. CONCLUSIONS

We propose a metamaterial, called magnetometamaterial, which can transport tiny particles. Being composed of a substrate on which cylindrical magnetic disks are placed in rows, this metamaterial, in analogy with electric materials, can operate as a conductor, a semiconductor, or an insulator, in transporting magnetic microparticles. To achieve the operating regimes, the proposed magnetometamaterial, in 1D format, needs to be biased by adjusting the applied external magnetic field frequency. In the conducting regime, all the particles move along the magnetic tracks, while in the semiconducting regime, some particles move and some others do not. We examine the percentage of moving particles (i.e., conductivity) in various frequencies and gap sizes. In an insulating regime, all particles move around single magnets. We discuss the effects of various parameters, including the particle size, the magnetic susceptibility of the particle, the disk size, and the fluid viscosity on the conductivity of the introduced magnetometamaterial. We also study the 2D format. We show that application of an in-plane external magnetic field results only in closed-loop particle trajectories. To transport particles in open loops, in addition to the rotating in-plane field, a modulated vertical bias field is needed. We show that in the 2D magnetometamaterials, particle transports with arbitrary trajectories are achievable. The proposed metamaterial allows us to manipulate a large number of particles in parallel, and all particles are synced with the external rotating magnetic field. In the conducting regime, the magnetic particle current is proportional to the frequency of the external magnetic field, which resembles Ohm's law in the electric conductors. This chip has potential applications in lab-on-a-chip systems and single-cell analysis tools.

The data that supports the findings of this study are available within the article.

[1] D. P. Ryan, Y. Chen, P. Nguyen, P. M. Goodwin, J. W. Carey, Q. Kang, J. H. Werner, and H. S. Viswanathan,

3D particle transport in multichannel microfluidic networks with rough surfaces, Sci. Rep. **10**, 13848 (2020).

[2] R. Abedini-Nassab and N. Mahdaviyan, A microfluidic platform equipped With magnetic nano films for organizing Bio-particle arrays and long-term studies, IEEE Sens. J. **20**, 9668 (2020).

[3] R. Abedini-Nassab, Magnetomicrofluidic platforms for organizing arrays of single-particles and particle-pairs, J. Microelectromech. Syst. **28**, 732 (2019).

[4] M. Baudoin, J. L. Thomas, R. A. Sahely, J. C. Gerbedoen, Z. Gong, A. Sivery, O. B. Matar, N. Smagin, P. Favreau, and A. Vlandas, Spatially selective manipulation of cells with single-beam acoustical tweezers, Nat. Commun. **11**, 4244 (2020).

[5] R. Abedini-Nassab, D. Y. Joh, M. Van Heest, C. Baker, A. Chilkoti, D. M. Murdoch, and B. B. Yellen, Magnetophoretic conductors and diodes in a 3D magnetic field, Adv. Funct. Mater. **26**, 4026 (2016).

[6] D. Di Carlo, D. Irimia, R. G. Tompkins, and M. Toner, Continuous inertial focusing, ordering, and separation of particles in microchannels, Proc. Natl. Acad. Sci. U. S. A. **104**, 18892 (2007).

[7] J. Cha and I. Lee, Single-cell network biology for resolving cellular heterogeneity in human diseases, Exp. Mol. Med. **52**, 1798 (2020).

[8] M. Mantri, G. J. Scuderi, R. Abedini-Nassab, M. F. Z. Wang, D. McKellar, H. Shi, B. Grodner, J. T. Butcher, and I. De Vlaminck, Spatiotemporal single-cell RNA sequencing of developing chicken hearts identifies interplay between cellular differentiation and morphogenesis, Nat. Commun. **12**, 1771 (2021).

[9] F. Wu, J. Fan, Y. He, A. Xiong, J. Yu, Y. Li, Y. Zhang, W. Zhao, F. Zhou, W. Li, *et al.*, Single-cell profiling of tumor heterogeneity and the microenvironment in advanced non-small cell lung cancer, Nat. Commun. **12**, 2540 (2021).

[10] Y. Zhang, S. P. Narayanan, R. Mannan, G. Raskind, X. Wang, P. Vats, F. Su, N. Hosseini, X. Cao, C. Kumar-Sinha, *et al.*, Single-cell analyses of renal cell cancers reveal insights into tumor microenvironment, cell of origin, and therapy response, Proc. Natl. Acad. Sci. U. S. A. **118**, e2103240118 (2021).

[11] D. A. Lawson, K. Kessenbrock, R. T. Davis, N. Pervolarakis, and Z. Werb, Tumour heterogeneity and metastasis at single-cell resolution, Nat. Cell Biol. **20**, 1349 (2018).

[12] S. W. Kazer, T. P. Aicher, D. M. Muema, S. L. Carroll, J. Ordovas-Montanes, V. N. Miao, A. A. Tu, C. G. K. Ziegler, S. K. Nyquist, E. B. Wong, *et al.*, Integrated single-cell analysis of multicellular immune dynamics during hyperacute HIV-1 infection, Nat. Med. **26**, 511 (2020).

[13] R. Liu, Y. J. Yeh, A. Varabyou, J. A. Collora, S. Sherrill-Mix, C. C. Talbot, S. Mehta, K. Albrecht, H. Hao, H. Zhang, *et al.*, Single-cell transcriptional landscapes reveal HIV-1-driven aberrant host gene transcription as a potential therapeutic target, Sci. Transl. Med. **12**, eaaz0802 (2020).

[14] E. Stephenson, G. Reynolds, R. A. Botting, F. J. Calero-Nieto, M. D. Morgan, Z. K. Tuong, K. Bach, W. Sungnak, K. B. Worlock, M. Yoshida, *et al.*, Single-cell multi-omics analysis of the immune response in COVID-19, Nat. Med. **27**, 904 (2021).

[15] N. Liu, C. Jiang, P. Cai, Z. Shen, W. Sun, H. Xu, M. Fang, X. Yao, L. Zhu, X. Gao, *et al.*, Single-cell analysis of COVID-19, sepsis, and HIV infection reveals hyperinflammatory and immunosuppressive signatures in monocytes, Cell Rep. **37**, 109793 (2021).

[16] A. F. Malone and B. D. Humphreys, Single-cell transcriptomics and solid organ transplantation, Transplantation **103**, 1776 (2019).

[17] Q. Zhuang, H. Li, B. Peng, Y. Liu, Y. Zhang, H. Cai, S. Liu, and Y. Ming, Single-Cell transcriptomic analysis of peripheral blood reveals a novel B-cell subset in renal allograft recipients With accommodation, Front. Pharmacol. **12**, 706580 (2021).

[18] E. Z. Macosko, A. Basu, R. Satija, J. Nemesh, K. Shekhar, M. Goldman, I. Tirosh, A. R. Bialas, N. Kamitaki, E. M. Martersteck, *et al.*, Highly parallel genome-wide expression profiling of individual cells using nanoliter droplets, Cell **161**, 1202 (2015).

[19] A. M. Klein, L. Mazutis, I. Akartuna, N. Tallapragada, A. Veres, V. Li, L. Peshkin, D. A. Weitz, and M. W. Kirschner, Droplet barcoding for single-cell transcriptomics applied to embryonic stem cells, Cell **161**, 1187 (2015).

[20] J. Brummelman, C. Haftmann, N. G. Núñez, G. Alvisi, E. M. C. Mazza, B. Becher, and E. Lugli, Development, application and computational analysis of high-dimensional fluorescent antibody panels for single-cell flow cytometry, Nat. Protoc. **14**, 1946 (2019).

[21] J. C. Love, J. L. Ronan, G. M. Grotenbreg, A. G. van der Veen, and H. L. Ploegh, A microengraving method for rapid selection of single cells producing antigen-specific antibodies, Nat. Biotechnol. **24**, 703 (2006).

[22] D. Di Carlo, L. Y. Wu, and L. P. Lee, Dynamic single cell culture array, Lab Chip **6**, 1445 (2006).

[23] Q. Luan, C. Macaraniag, J. Zhou, and I. Papautsky, Microfluidic systems for hydrodynamic trapping of cells and clusters, Biomicrofluidics **14**, 031502 (2020).

[24] M. Wu, A. Ozcelik, J. Rufo, Z. Wang, R. Fang, and T. Jun Huang, Acoustofluidic separation of cells and particles, Microsyst. Nanoeng. **5**, 32 (2019).

[25] R. Abedini-Nassab, S. M. Emami, and A. N. Nowghabi, Nanotechnology and acoustics in medicine and biology, Recent Pat. Nanotechnol. (2021).

[26] M. M. Wang, E. Tu, D. E. Raymond, J. M. Yang, H. Zhang, N. Hagen, B. Dees, E. M. Mercer, A. H. Forster, I. Kariv, *et al.*, Microfluidic sorting of mammalian cells by optical force switching, Nat. Biotechnol. **23**, 83 (2005).

[27] M. Punjiya, H. R. Nejad, J. Mathews, M. Levin, and S. Sonkusale, A flow through device for simultaneous dielectrophoretic cell trapping and AC electroporation, Sci. Rep. **9**, 11988 (2019).

[28] K. Samlali, F. Ahmadi, A. B. V. Quach, G. Soffer, and S. C. C. Shih, One cell, One drop, One click: Hybrid microfluidics for mammalian single cell isolation, Small **16**, e2002400 (2020).

[29] S. Kim, F. Qiu, A. Ghanbari, C. Moon, L. Zhang, B. J. Nelson, and H. Choi, Fabrication and characterization of magnetic microrobots for three-dimensional cell culture and targeted transportation, Adv. Mater. **25**, 5863 (2013).

[30] O. Lefebvre, H. H. Cao, M. Cortés Francisco, M. Woytasik, E. Dufour-Gergam, M. Ammar, and E. Martincic, Reusable embedded microcoils for magnetic nano-beads trapping in microfluidics: Magnetic simulation and experiments, Micromachines **11**, 257 (2020).
[31] M. Kadic, G. W. Milton, M. van Hecke, and M. Wegener, 3D metamaterials, Nat. Rev. Phys. **1**, 198 (2019).
[32] S. Bonfanti, R. Guerra, F. Font-Clos, D. Rayneau-Kirkhope, and S. Zapperi, Automatic design of mechanical metamaterial actuators, Nat. Commun. **11**, 4162 (2020).
[33] C. Cho, X. Wen, N. Park, and J. Li, Digitally virtualized atoms for acoustic metamaterials, Nat. Commun. **11**, 251 (2020).
[34] M. Z. Yaqoob, A. Ghaffar, M. A. S. Alkanhal, M. Y. Naz, A. H. Alqahtani, and Y. Khan, Electromagnetic surface waves supported by a resistive metasurface-covered metamaterial structure, Sci. Rep. **10**, 15548 (2020).
[35] J. Y. Yin and T. J. Cui, Metamaterial lenses, Wiley Encyclopedia of Electrical and Electronics Engineering (2019), p. 1.
[36] A. Salim and S. Lim, Review of recent metamaterial microfluidic sensors, Sensors **18**, 232 (2018).
[37] Z. Geng, X. Zhang, Z. Fan, X. Lv, and H. Chen, A route to terahertz metamaterial biosensor integrated with microfluidics for liver cancer biomarker testing in early stage, Sci. Rep. **7**, 16378 (2017).
[38] X. Zhao, G. Duan, A. Li, C. Chen, and X. Zhang, Integrating microsystems with metamaterials towards metadevices, Microsyst. Nanoeng. **5**, 5 (2019).
[39] K. E. McCloskey, J. J. Chalmers, and M. Zborowski, Magnetic cell separation: Characterization of magnetophoretic mobility, Anal. Chem. **75**, 6868 (2003).
[40] A. O. Ayansiji, A. V. Dighe, A. A. Linninger, and M. R. Singh, Constitutive relationship and governing physical properties for magnetophoresis, Proc. Natl. Acad. Sci. U. S. A. **117**, 30208 (2020).
[41] J. Lim, C. Lanni, E. R. Evarts, F. Lanni, R. D. Tilton, and S. A. Majetich, Magnetophoresis of nanoparticles, ACS Nano **5**, 217 (2011).
[42] S. S. Leong, Z. Ahmad, and J. Lim, Magnetophoresis of superparamagnetic nanoparticles at low field gradient: Hydrodynamic effect, Soft Matter **11**, 6968 (2015).
[43] J. Gómez-Pastora, I. H. Karampelas, E. Bringas, E. P. Furlani, and I. Ortiz, Numerical analysis of bead magnetophoresis from flowing blood in a continuous-flow microchannel: Implications to the bead-fluid interactions, Sci. Rep. **9**, 7265 (2019).
[44] S. R. Goudu, H. Kim, X. Hu, B. Lim, K. Kim, S. R. Torati, H. Ceylan, D. Sheehan, M. Sitti, and C. Kim, Mattertronics for programmable manipulation and multiplex storage of pseudo-diamagnetic holes and label-free cells, Nat. Commun. **12**, 3024 (2021).
[45] M. Zborowski, G. R. Ostera, L. R. Moore, S. Milliron, J. J. Chalmers, and A. N. Schechter, Red blood cell magnetophoresis, Biophys. J. **84**, 2638 (2003).
[46] S. Miltenyi, W. Müller, W. Weichel, and A. Radbruch, High gradient magnetic cell separation with MACS, Cytometry **11**, 231 (1990).
[47] A. Munaz, M. J. A. Shiddiky, and N. T. Nguyen, Recent advances and current challenges in magnetophoresis based micro magnetofluidics, Biomicrofluidics **12**, 031501 (2018).
[48] A. Shamloo, A. Naghdloo, and M. Besanjideh, Cancer cell enrichment on a centrifugal microfluidic platform using hydrodynamic and magnetophoretic techniques, Sci. Rep. **11**, 1939 (2021).
[49] S. R. Goudu, X. Hu, B. Lim, K. Kim, H. Kim, J. Yoon, and C. Kim, Characterization of superparamagnetic particles mobility by On-chip micromagnets, IEEE Trans. Magn. **54**, 1 (2018).
[50] X. Hu, R. Abedini-Nassab, B. Lim, Y. Yang, M. Howdyshell, R. Sooryakumar, B. B. Yellen, and C. Kim, Dynamic trajectory analysis of superparamagnetic beads driven by on-chip micromagnets, J. Appl. Phys. **118**, 203904 (2015).
[51] Y. Ouyang, M. A. Tahir, D. J. Lichtenwalner, and B. B. Yellen, Origin of multiplexing capabilities of multifrequency magnetic ratchets, Phys. Rev. E: Stat., Nonlinear, Soft Matter Phys. **85**, 041407 (2012).
[52] L. Gao, M. A. Tahir, L. N. Virgin, and B. B. Yellen, Multiplexing superparamagnetic beads driven by multifrequency ratchets, Lab Chip **11**, 4214 (2011).
[53] D. Lips, R. L. Stoop, P. Maass, and P. Tierno, Emergent colloidal currents across ordered and disordered landscapes, Commun. Phys. **4**, 224 (2021).
[54] M. A. Tahir, L. Gao, L. N. Virgin, and B. B. Yellen, Transport of superparamagnetic beads through a two-dimensional potential energy landscape, Phys. Rev. E: Stat., Nonlinear, Soft Matter Phys. **84**, 011403 (2011).
[55] L. Li, R. Abedini-Nassab, and B. B. Yellen, Monolithically integrated helmholtz coils by 3-dimensional printing, Appl. Phys. Lett. **104**, 253505 (2014).
[56] B. Lim, V. Reddy, X. Hu, K. Kim, M. Jadhav, R. Abedini-Nassab, Y. W. Noh, Y. T. Lim, B. B. Yellen, and C. Kim, Magnetophoretic circuits for digital control of single particles and cells, Nat. Commun. **5**, 3846 (2014).
[57] R. Abedini-Nassab, Thesis, Duke University, Durham (2017), p. 753.
[58] J. A. Stratton, *Electromagnetic Theory* (McGraw Hill Book Company, New York, London, 1941).
[59] See Supplemental Material at http://link.aps.org/supplemental/10.1103/PhysRevApplied.17.014020 for the particle trajectory at the phase-locked regime.